



Research Paper

Design of an additively manufactured functionally graded material of 316 stainless steel and Ti-6Al-4V with Ni-20Cr, Cr, and V intermediate compositions

Lourdes D. Bobbio^a, Brandon Bocklund^a, Emrah Simsek^b, Ryan T. Ott^b, Matt J. Kramer^b, Zi-Kui Liu^a, Allison M. Beese^{a,c,*}

^a Department of Material Science and Engineering, Pennsylvania State University, University Park, PA 16802, United States

^b Division of Materials Sciences and Engineering, Ames Laboratory, Iowa State University, Ames, IA 50011, United States

^c Department of Mechanical Engineering, Pennsylvania State University, University Park, PA 16802, United States

ARTICLE INFO

Keywords:

Additive manufacturing
Thermodynamic modeling
Functionally graded material (FGM)
Solidification
Alloys

ABSTRACT

This study presents a method for designing a computationally informed gradient pathway to fabricate a functionally graded material (FGM) with terminal alloys of 316 stainless steel (SS316) and Ti-6Al-4V via directed energy deposition additive manufacturing with powder feedstock. The grading is accomplished through the introduction of intermediate elements and alloys (Ni-20Cr, Cr, and V) to avoid the brittle Fe-Ti intermetallic phases that form in the direct liquid phase joining of Ti-alloys and stainless steels. Using a combination of equilibrium calculations and Scheil-Gulliver simulations, a compositional pathway was designed to avoid deleterious phases. FGM samples were fabricated and experimentally characterized to determine the viability of the pathway. A change in phases from fcc to bcc was predicted to occur within the Ni-20Cr/Cr gradient region, and this was validated through experimental characterization. No detrimental phases (intermetallic, Laves, or σ phases) formed along the gradient path, demonstrating a successful computationally-informed design and fabrication of an FGM from SS316 to Ti-6Al-4V.

1. Introduction

Functionally graded materials (FGMs) made by additive manufacturing (AM) have compositions, mesostructures, and/or microstructures that vary as a function of position [1–3], resulting in spatial variation in properties (e.g., mechanical, thermal, magnetic) [2, 4, 5]. FGMs have the potential to be used as an alternative to more conventional ways of combining dissimilar materials, e.g., through welding, mechanical fasteners, or interlocks, which present local abrupt changes in properties. FGMs also have the potential to enable the fabrication of multifunctional components with specially designed spatially tailored properties, as has been discussed in recent review papers [1, 2].

The joining of stainless steel and titanium alloys is of interest in the aerospace [6, 7] and nuclear industries [8, 9] for the strength and corrosion resistance of both alloys, as well as titanium's low density, which provides avenues for lightweighting; however, combining stainless steel with titanium and its alloys through liquid phase joining and

friction stir welding, has been shown to be problematic due to the formation of intermetallic phases during liquid phase mixing of these two alloy systems [7, 8, 10–13]. These intermetallic phases (e.g., B2 and Laves C14 phases), commonly result in cracking and/or delamination during the fabrication process [1, 14–17]. Even samples that have no major defects in the as-built condition can have cracks form during post-processing heat treatments due to growth of detrimental phases or additional thermal stresses [18].

Sahasrabudhe et al. [14] examined directly joining Ti-6Al-4V and stainless steel 316 L (SS316L) using directed energy deposition (DED). X-ray diffraction (XRD) analysis revealed the presence of FeTi (B2), Fe₂Ti, and Cr₂Ti (Laves) intermetallic phases at the interface between SS316 and Ti-6Al-4V, which resulted in microcracks. In order to mitigate the effects of directly joining Ti and Ti-alloys with stainless steel, intermediate elements have been studied as potential buffer layers to prevent the direct liquid mixing of Ti and Fe that results in intermetallic phase formation. Examples of these include Ni [19], NiCr [14], V [1, 20–23], and Cu [24]. Li et al. graded between SS316L and Ti-6Al-4V

* Corresponding author at: Department of Material Science and Engineering, Pennsylvania State University, University Park, PA 16802, United States.
E-mail address: amb961@psu.edu (A.M. Beese).

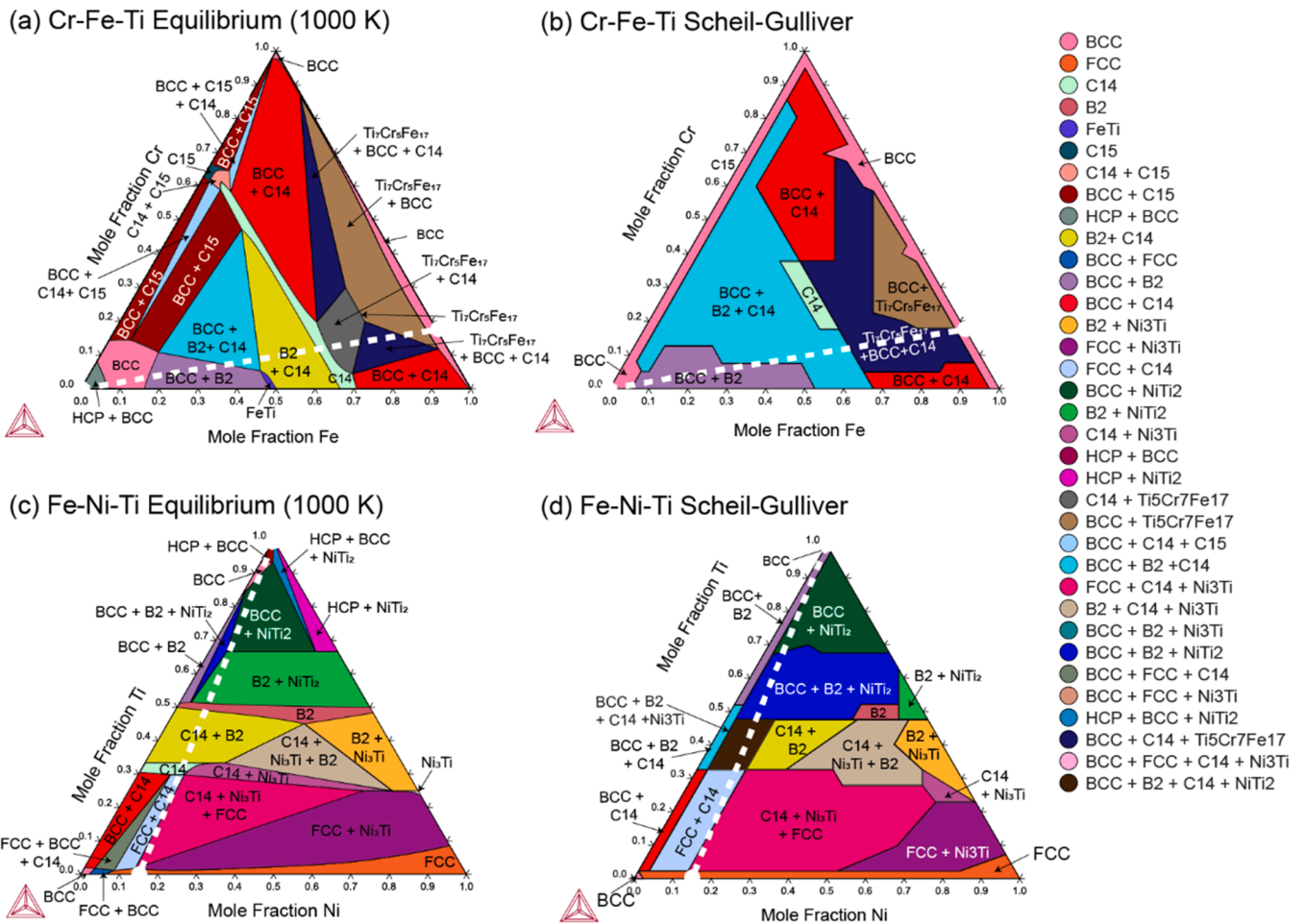


Fig. 1. Ternary diagrams showing composition regions for the formation of various phases (represented by different colors) across the full composition space of the (a,b) Cr-Fe-Ti [37] and (c,d) Fe-Ni-Ti [36] systems. The white dashed lines indicate the direct linear pathway between Ti and an approximated stainless steel alloy.

Table 1

Thermodynamic assessments used to evaluate feasibility for the ternary sub-systems of the Cr-Fe-Ni-Ti-V five component system used in Fig. 1.

Ternary sub-system	Source of thermodynamic assessment
Cr-Fe-Ni	[40]
Cr-Fe-Ti	[37]
Cr-Fe-V	[41]
Cr-Ni-Ti	[42]
Cr-Ni-V	[41]
Cr-Ti-V	[43]
Fe-Ni-Ti	[36]
Fe-Ni-V	[44]
Fe-Ti-V	[45]
Ni-Ti-V	[46]

through depositing pure layers of Fe, Cr, and V onto a SS316L baseplate [21]. No Fe-Ti intermetallic compounds formed, and while σ phase had the potential to form between the Fe and Cr regions, the authors cited the high cooling rates of AM as suppressing the formation of σ phase in the FGM. In this case, the (Fe,Cr) solid solution was kinetically frozen in, but is not expected to be thermodynamically stable.

In the aforementioned study by Sahasrabudhe et al., the authors also fabricated a sample that used a NiCr bond layer between the Ti-6Al-4V and SS316 layers. XRD analysis showed evidence of Cr_2Ti at the interface between NiCr and Ti-6Al-4V. While no microcracks or other defects were found in this sample, Cr_2Ti is a brittle intermetallic phase that could result in cracking [14,25]. Using NiCr as an interlayer between

stainless steel and titanium has been shown to have other problematic effects. Liu et al. [19] examined Ni-based superalloy/Ni80Cr20 laminated composites that were diffusion bonded, with different bonding times, to Ti-6Al-4V baseplates, showing that all samples had the NiTi, Ni_3Ti , and NiTi_2 phases at the interface.

Vanadium is another interlayer element that has been studied both for joining Ti and stainless steel through welding and additive manufacturing. Zhang et al. [20] studied the use of V as an interlayer in a Ti-alloy and stainless steel joint fabricated through pulsed laser welding, successfully avoiding the formation of Fe-Ti intermetallics. XRD analysis showed the formation of a (Fe,V) solid solution, which, at certain compositions could form the FeV- σ phase [26,27]; however, due to the high fraction of Fe in this study, FeV- σ phase formation was avoided.

Avoiding σ phase formation is not always possible when combining V with stainless steel. In a study on welding 17-4PH stainless steel and V, different weld line offsets were studied in order to regulate the V concentration, and therefore, the formation of σ phase [18]. Composition analysis showed that the amount of V ranged from 15 at% for the samples with the larger offset to 40 at% for the samples with the smaller offset. The as-welded samples contained (Fe,V) solid solution, and electron backscatter diffraction (EBSD) analysis confirmed the formation of bcc phase. However, after heat treatment at 600 °C for 12 h, EBSD analysis showed a high concentration of σ phase for all samples. In a study on σ phase formation in two different stainless steel and V FGMs, Bobbio et al. highlighted the importance of time spent within the favorable temperature range for σ phase growth during directed energy

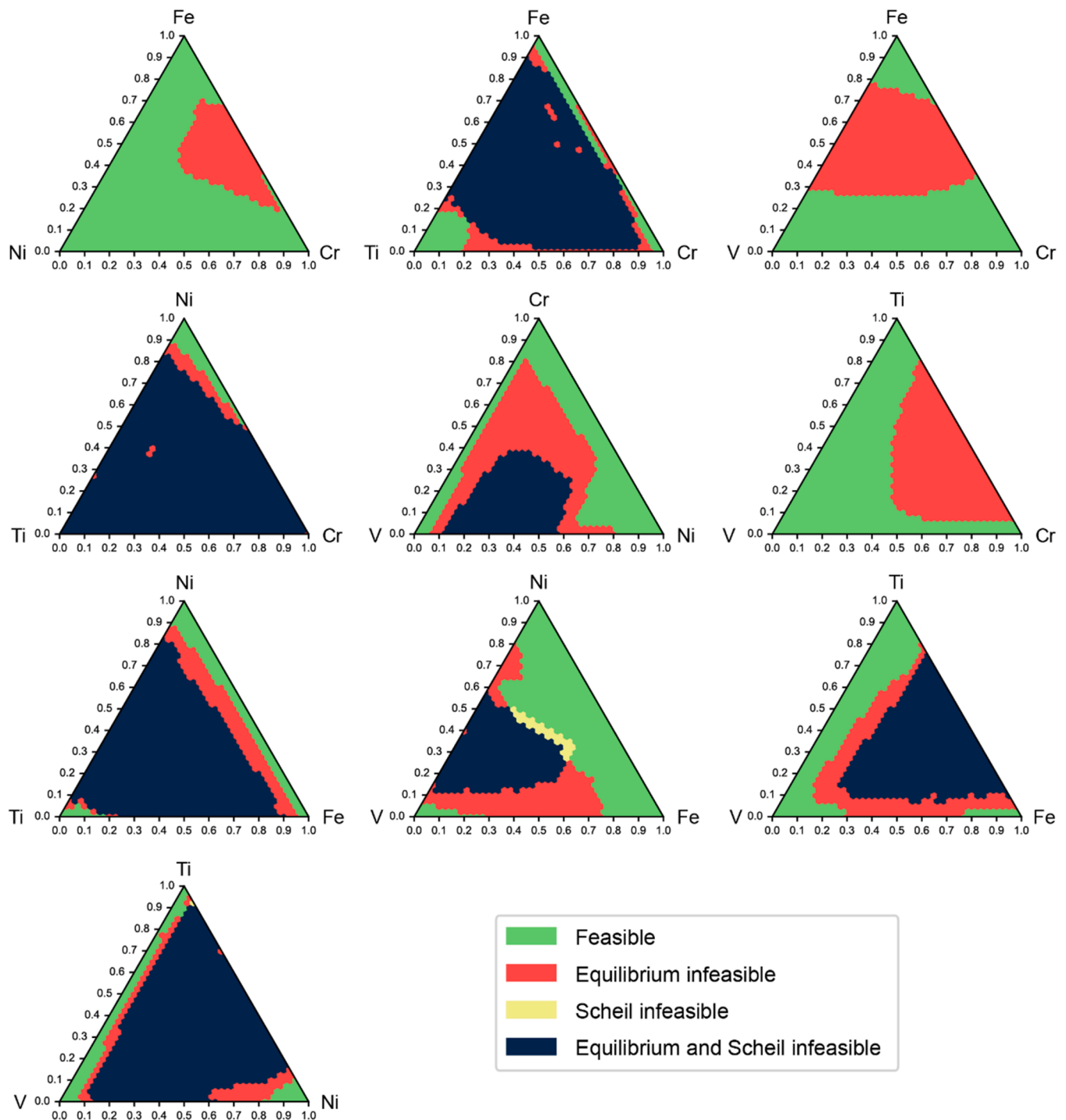


Fig. 2. Ternary plots representing the feasibility, in terms of absence of detrimental phases, of composition in the examined ternary systems to grade between SS316L and Ti-6Al-4V (Cr-Ti-V, Cr-Ni-V, Cr-Fe-Ni, Cr-Fe-V, Fe-Ni-Ti, and Fe-Ni-V). Compositions in green have under 10 at% of a detrimental phase, and are denoted as feasible, while compositions in red are deemed infeasible due to having 10% or greater of a detrimental phase as calculated through equilibrium or Scheil simulations.

deposition (DED) AM [28]. Experimental characterization and computational modeling showed that the primary factor for σ phase growth was thermal history as, at similar compositions, regions that were subjected to elevated temperatures for longer times due to their location being above cracked regions had ~ 10 times more σ phase than those that cooled faster. This finding, combined with the results from the study by Adomako et al. [18] highlights that both time and temperature are factors in σ phase formation and growth.

The presence of brittle intermetallic phases in FGMs generally results

in regions of higher hardness and reduced ductility [14,15]. For example, Adomako et al. [18] examined the hardness in the fusion zone of three welded 17-4PH and V samples in which the weld line was offset. The average hardness ranged from 342 HV to 440 HV depending on the weld line offset, where the sample with the smaller offset (and higher V content) had a higher hardness and the sample with the larger offset (and lower V content) had a lower hardness. After post-weld heat treatment, EBSD and XRD analysis revealed that the fusion zone had significant amounts of σ phase, which resulted in a higher hardness in

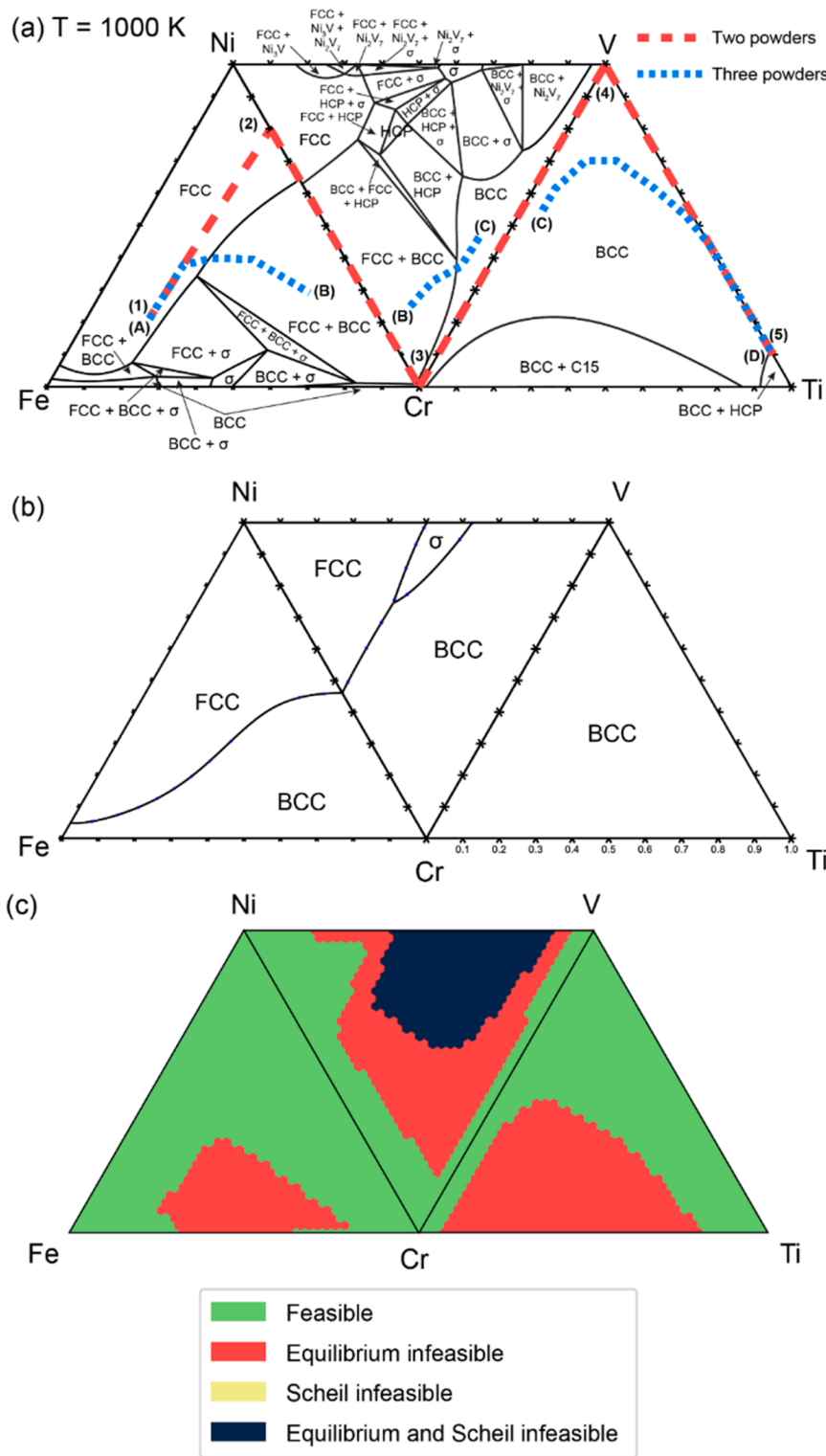


Fig. 3. (a) Ternary phase diagrams of the Cr-Ni-Fe, Cr-Ni-V, and Cr-Ti-V systems showing the two-powder gradient pathway used for this study (red dashed lines) and a potential gradient pathway if varying three powders at a time (blue dotted lines). (b) Liquidus projections for the same three systems showing the monovariant lines dividing the fcc, bcc, and σ regions of the liquidus diagrams. (c) Ternary feasibility diagrams showing the designed pathway based on equilibrium calculations and Scheil simulations.

this region (approximately 1000 HV), and a much lower ductility compared to the as-welded samples.

Equilibrium calculations through the CALculation of PHase Diagrams (CALPHAD) method have been used as a tool with which to predict phase compositions in FGMs made by AM [1,2,15]. CALPHAD-based equilibrium calculations have been paired with path planning algorithms to find optimized gradient composition pathways that avoid detrimental phases [29,30]. Kirk et al. [29] developed an algorithm that was then experimentally validated by Eliseeva et al. [30].

Their method used a rapidly-exploring random tree class of algorithms to design compositional pathways that avoid undesirable phases that are expected between room temperature and the manufacturing temperature. Using this algorithm, the authors found an idealized non-linear path between 316 L stainless steel and pure Cr that avoided σ phase, which they validated experimentally. This method is based on equilibrium conditions and while it considers a wide range of temperatures, it does not consider phase transformations during solidification.

As AM is a far-from-equilibrium process, the direct applicability of

Table 2

Melting and liquidus temperatures of constituent major alloys/elements in the FGM.

Alloy/Element	Melting/Liquidus Temperature (K)
SS316	1673
NiCr	1673
Cr	2136 [47]
V	2188
Ti-6Al-4V	1933

equilibrium calculations is limited. In contrast, Scheil-Gulliver solidification simulations (referred to here as Scheil simulations) have been applied to AM as a method of assessing the predicted solidification products in FGM systems. This allows for non-equilibrium solidification modeling that can better capture the fast cooling of additive manufacturing. Bocklund et al. [31] showed that Scheil solidification simulations better predicted experimentally observed phase fractions than equilibrium calculations when assessing gradients of both Ti-6Al-4V to Invar 36 and commercially pure Ti to Invar 36 FGMs. In short, computationally, both Scheil simulations and equilibrium calculations represent thermodynamic limits: Scheil simulations are an upper limit for solidification-driven segregation, while equilibrium calculations represent the limiting equilibrium state of solid-state transformations. In reality, it is unlikely that either of these limits will be fully realized in the AM process and this could account for deviations between predicted and observed phases and phase compositions.

The goal of this study was to design a compositional pathway along which to grade between 316 stainless steel (SS316) and Ti-6Al-4V that avoids deleterious phase formation. This design was informed by thermodynamic modeling of the representative systems considering equilibrium calculations and Scheil solidification simulations to determine phase compositions within potentially relevant ternary systems. The gradient pathway, involving varying the volume fraction of two feedstock powders at a time, was designed to grade between SS316 and Ti-6Al-4V through intermediate grading to Ni-20Cr (henceforth referred to as NiCr), Cr, and V. The elemental and phase fractions of these gradients were experimentally evaluated, and good agreement was found between the planned gradient pathway and the deposited FGM.

2. Computational design of gradient pathway

To design a compositional pathway along which to grade between SS316 and Ti-6Al-4V, the phase compositions in the ternaries (Cr-Fe-Ti and Fe-Ni-Ti) comprising the major elements in each alloy were

evaluated using the CALPHAD method. This was done to determine if there were any feasible pathways along which to grade linearly or nonlinearly between the two terminal alloys while also avoiding deleterious phases. The CALPHAD method uses the Gibbs energy of individual phases parameterized with the multicomponent compound energy formalism in the form of sublattice models [32–34]. Both equilibrium and Scheil simulations were performed on a direct linear path between the two alloys as well as the full ternary systems. Both types of analyses were performed with pycalphad [35] using two databases – a database developed by Dekeyser et al. to analyze the Fe-Ni-Ti system [36] and a database developed by Wang et al. to analyze the Cr-Fe-Ti system [37]. Scheil simulations were performed to predict the solid phases that would precipitate from the melt during rapid solidification in AM. The scheil module of pycalphad, developed by this team, was used for these simulations [31,38]. This open-source solidification simulation tool can simulate both equilibrium and Scheil solidification and can distinguish ordered and disordered configurations of phases.

The Cr-Fe-Ti and Fe-Ni-Ti ternary diagrams are shown in Fig. 1, depicting the composition regions for formation of various phases that were predicted for equilibrium calculations at 1000 K (Fig. 1a for the Cr-Fe-Ti system and Fig. 1c for the Fe-Ni-Ti system) and Scheil simulations (Fig. 1b for the Cr-Fe-Ti system and Fig. 1d for the Fe-Ni-Ti system). The direct linear gradient pathway is marked by a white dashed line in all four diagrams. The results from these calculations show the intermediate phases (B2, C14) that form along a linear gradient path that would be detrimental to the structural integrity of an FGM directly grading between SS316 and Ti-6Al-4V. All other possible pathways, either linear or non-linear, cross through regions of detrimental phase formation; therefore, intermediate alloys/elements are necessary to design an FGM with terminal alloys of SS316 and Ti-6Al-4V.

All ten ternary sub-systems in the five component Cr-Fe-Ni-Ti-V system were evaluated to determine the feasibility of using different elements or alloys as intermediates between SS316 and Ti-6Al-4V using equilibrium calculations and Scheil simulations. The thermodynamic databases used for each ternary system are listed in Table 1. To capture all kinetically relevant phase transformations, the equilibrium calculations were performed between 1000 K and 2200 K (where all candidate alloy compositions are predicted to be liquid, see Table 2). This temperature range is based on the assumption that there will be no solid state phase transformations below 1000 K as the kinetics of phase transformation would be too slow [39]. A composition is considered feasible if all equilibrium calculations and the Scheil solidification simulation for the composition contains less than 10 at. % of a detrimental phase, i.e., any intermetallic or partially/fully-ordered solution

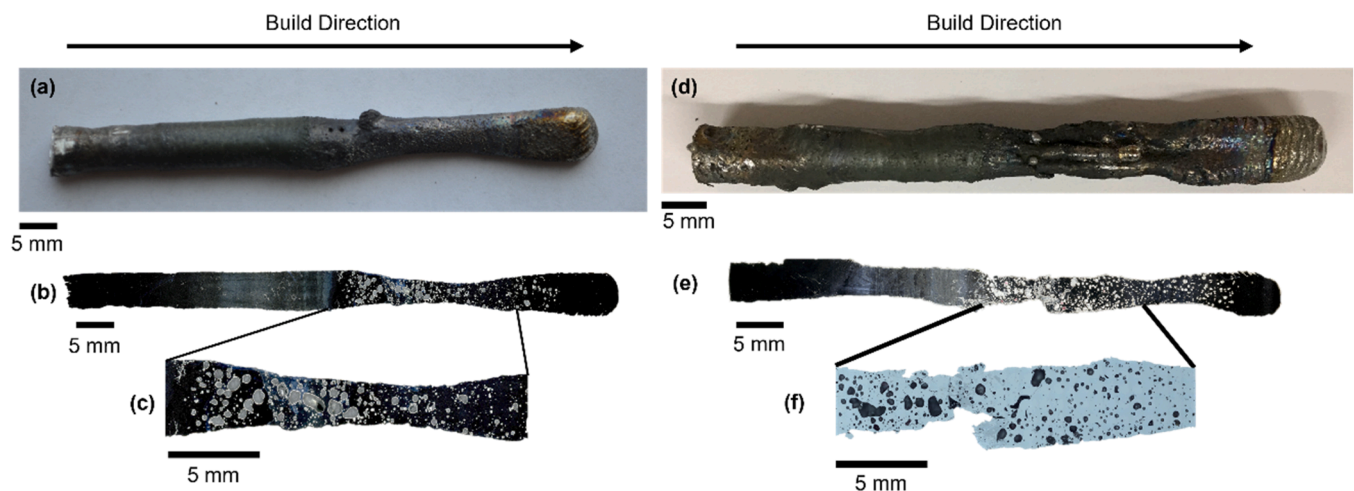


Fig. 4. (a, d) Photographs of the SS316/NiCr/Cr/V/Ti-6Al-4V FGM samples after removal from the baseplate. Optical microscope images of (b, e) the cross-section of the entire sample and (c, f) the portions of the samples with a high density of porosity. The build direction is denoted by arrows above (a) and (d).

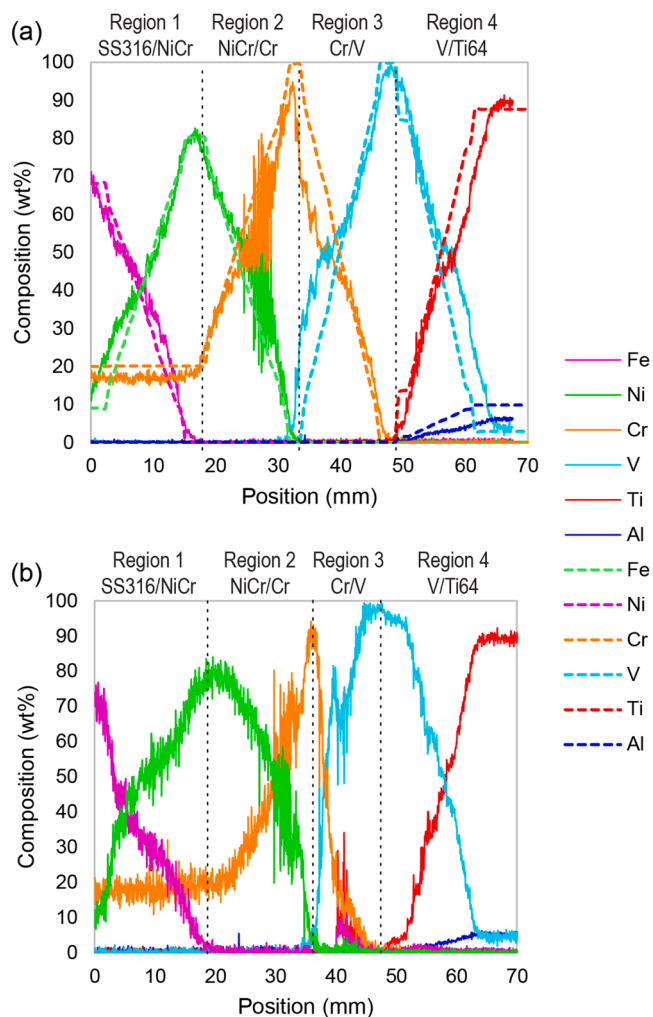


Fig. 5. Composition as a function of position along the height of the two FGM samples that were experimentally characterized. The EDS line scan in (a) corresponds to the sample in Fig. 4a and the line scan in (b) corresponds to Fig. 4b. The dashed lines indicate the planned deposited composition while the solid lines indicate the composition measured by EDS line scans. The four regions are marked by grey vertical dotted lines.

phase. We note that this cutoff of 10 at.% is not a strict requirement, but rather is a heuristic parameter used as a starting point for FGM design. Lowering the tolerated amount of detrimental phases expands the regions of infeasibility into the possible design space. In each ternary system, an evenly spaced grid of 861 candidate compositions on the ternary simplex were considered. Fig. 2c shows the regions of feasibility in each ternary system where feasible compositions are represented as green regions, compositions that are infeasible by equilibrium calculations are represented as red, compositions that are infeasible by Scheil solidification simulations are represented as yellow, and compositions that are infeasible by both equilibrium and Scheil simulations are represented as blue.

Visually inspecting the ternary feasibility diagrams in Fig. 2c makes it immediately clear which candidate systems may be useful for FGM design by noting the corners and edges of the diagram that are connected by contiguous feasible regions. For example, V is the only element of Cr, Fe, Ni, or V that shares a feasible edge with Ti, only Cr and Ti share feasible edges with V, and only Ni and V share feasible edges with Cr. Therefore, it can be concluded that the only viable thermodynamically stable pathway in Cr-Fe-Ni-Ti-V to join SS316 with Ti-6Al-4V requires passing through the Ni-Cr, Cr-V, and V-Ti binary edges. The path passing through these binary edges can be represented using the Cr-

Fe-Ni, Cr-Ni-V, and Cr-Ti-V systems shown in Fig. 3a. Pure Cr and V elemental metals and the Ni-20Cr alloy were selected as intermediates. The pathway segments go linearly from the 100% compositions of the constituent alloys and elements as follows (1) SS316 to (2) NiCr to (3) Cr (4) V to (5) Ti-6Al-4V.

In order to predict the phase relations in all four gradient regions of the SS316 to NiCr to Cr to V to Ti-6Al-4V FGM, equilibrium and Scheil calculations were performed as mentioned above. Three thermodynamic databases were used: an Cr-Fe-Ni database [40] was used for the Cr-Fe-Ni system, a Co-Cr-Fe-Ni-V database [41] was used for the Cr-Ni-V system, and an Cr-Ti-V database [43] was used for the Cr-Ti-V system. With this pathway, the only expected phases in the FGM were the fcc and bcc phases, with the transition from fcc to bcc occurring within the NiCr/Cr gradient region, and no detrimental phases were expected to form.

Note that the planned gradient pathway considers the ability to vary the relative amounts of two powders at a time, as was used in this study (see Section 3). DED systems with multiple powder feeders and the ability to simultaneously vary the volume fractions of more than two powders at a time could expand the design space for pathways with more compositional flexibility. To demonstrate this, an additional optimized gradient pathway was designed through CALPHAD analysis for a hypothetical system with the ability to vary the relative amounts of three powders simultaneously. This designed path is shown with a blue dotted line on the ternary phase diagrams in Fig. 3a. This pathway would allow for a smoother transition between gradient sections and would reduce the relative amounts of powder of each metal or alloy, condensing the vertical span of the gradient. The fabrication of such an FGM is beyond the scope of this work due to the present limitation in only being able to vary two powders at a time.

3. Experimental methods

Two pillar-shaped FGM samples were fabricated by vertically and linearly grading from SS316 to Ni-20Cr (Region 1), Ni-20Cr to Cr (Region 2), Cr to V (Region 3), and V to Ti-6Al-4V (Region 4) in incremental changes of about 5 vol%/layer in composition achieved through varying the powder feed rates from the four individual hoppers. The samples were fabricated using a DED AM system (Optomec LENS™) with an Ar environment (< 5 ppm O₂). The system utilizes 3-axis motion (x- and y-translation of the sample and z-translation of the print head) to fabricate 3D shapes. The Yb-fiber laser operated at a power that varied between 400 and 600 W (average power of 527 W). Given the large variation in melting temperatures of the constituent powder feedstocks (see Table 2), the power was adjusted automatically during fabrication using a melt pool sensor in the LENS system that varies the power to keep the melt pool size constant during fabrication. This resulted in an irregular shape of the build. Additional processing parameters were as follows: a 0.8 mm laser beam diameter, a hatch spacing of 0.38 mm, a step height of 0.254 mm, and a scan speed of 5.08 mm/s. The powders used for fabrication were: 316 L stainless steel (Carpenter Micro-Melt, 45–150 μm), Ni-20Cr powder (Atlantic Equipment Engineers, 45–88 μm), Cr powder (Atlantic Equipment Engineers, 53–150 μm), V powder (Atlantic Equipment Engineers, Inc., 44–105 μm), and Ti-6Al-4V powder (Advanced Powders & Coatings, 45–106 μm). The as-built samples are pictured in Fig. 4a and d and measured between 60 and 70 mm in height and approximately 6 mm in diameter, although the diameter was irregular.

The samples were mounted separately in epoxy resin and ground down using 180 grit SiC paper until the cross-section of the sample was revealed. The samples were then polished using standard metallographic techniques, with a final polish using 0.05 μm silica suspension. Optical microscope images of the cross-sectioned samples are shown in Fig. 4b and e.

The two samples were used for elemental and phase characterization, as well as hardness measurements. Energy dispersive X-ray

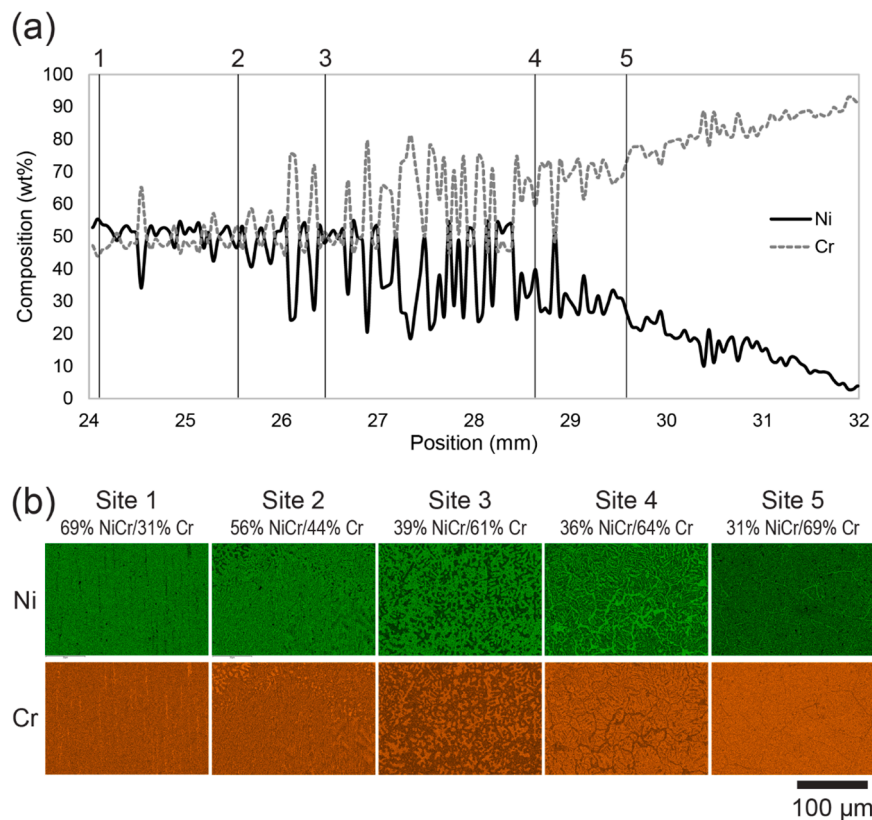


Fig. 6. (a) EDS line scan data along an 8 mm region between heights of 24 mm and 32 mm that highlights the section of Region 2 (NiCr/Cr) where spatial compositional fluctuations were present. (b) Local EDS area maps at five locations (Sites 1–5) within the 8 mm portion of Region 2 shown in (a) highlighting microstructural and elemental changes across Region 2. The gradient compositions are shown below each site name.

spectroscopy (EDS) was performed in a scanning electron microscope (SEM, Thermo-Scientific, Apreo S Low Vac, Massachusetts) with a silicon drift detector attachment (Oxford Instruments, Ultim Max silicon drift detector, Massachusetts) to measure the composition of the FGM through both line scans and area mapping. XRD was used for phase identification within each of the gradient regions of the FGM, and the diffraction patterns were collected using a Bragg-Brentano-type diffractometer (Panalytical, Empyrean, Cu K- α X-ray source, 45 kV, 40 mA, $\lambda = 1.54 \text{ \AA}$, 0.5° slit size, 5 mm mask, Malvern, UK). EBSD analysis (Oxford Instruments, Symmetry detector, Massachusetts) was performed on the NiCr/Cr gradient region of the sample, where computational analysis predicted a phase transition, to analyze local phase compositions. The Vickers microhardness was measured along the height of the FGM using a load of 100 gf and a loading time of 10 s (Leco, LM 110AT Hardness Tester, Michigan).

4. Results and discussion

The focus of the experimental analysis is on the NiCr/Cr gradient region (Region 2). Regions 1 and 4 have been previously studied and reported on (Bobbio et al. examined a stainless steel and NiCr FGM in [48] and Hofmann et al. examined a Ti-6Al-4V to V FGM in [2]). Given the complete solid solution in the Cr/V binary phase diagram, limited analysis was performed in this region.

4.1. Experimental results

Initial optical analysis of the samples showed a large area with a significant amount of porosity in the top half of the samples as shown in Fig. 4c and f. The pores varied in size and morphology, with some as large as 1 mm in the longest imaged dimension.

EDS line scans were performed along the entire height of both

samples to determine composition as a function of vertical position. A comparison of the planned versus experimentally measured composition of the sample in Fig. 4a is shown in Fig. 5a. The measured composition of the sample in Fig. 4b is shown in Fig. 5b, showing good agreement. The EDS line scans indicated that the onset of the porosity corresponded to the introduction of V in the Cr/V region in both samples. Note that the focus of this study is to determine if the proposed composition pathway is free of detrimental phase, and process optimization will be performed in the future.

Compositional fluctuations in Region 2 (NiCr/Cr) started at a layer composition of approximately 50 wt% Ni/50 wt% Cr and extended to a layer composition of approximately 30 wt% Ni/70 wt% Cr. This compositional gradient region is where the phase transition from the fcc phase to the bcc phase was anticipated based on the initial Scheil simulations. A detailed view of the composition variations and segregation in this section of the FGM is given in Fig. 6.

Fig. 7 shows XRD patterns from the center of each of the four gradient regions of the FGM. Each diffraction pattern spans an area of $6 \text{ mm} \times 7 \text{ mm}$, which covers a large portion of each gradient region. These diffraction patterns show transitions from a fcc single phase in Region 1 (SS316/NiCr) to a fcc/bcc two-phase mixture in Region 2 (NiCr/Cr), and finally to a bcc single phase in Regions 3 (Cr/V) and 4 (V/Ti-6Al-4V). The two-phase mixture in Region 2 corresponds to the same area where the Ni-Cr elemental segregation was observed via EDS.

EBSD analysis was performed at five locations within Region 2 (NiCr/Cr), where the fcc/bcc two-phase mixture was observed via XRD analysis and compositional fluctuations were observed in the EDS line scans. The resulting phase maps in Fig. 8 show the progression from primarily fcc phase to primarily bcc phase as the overall layer elemental composition changes from 56 wt% Ni/44 wt% Cr to 24 wt% Ni/76 wt% Cr, with an accompanying change in microstructure from a cellular structure in the fcc-rich regions to an equiaxed grain morphology in the

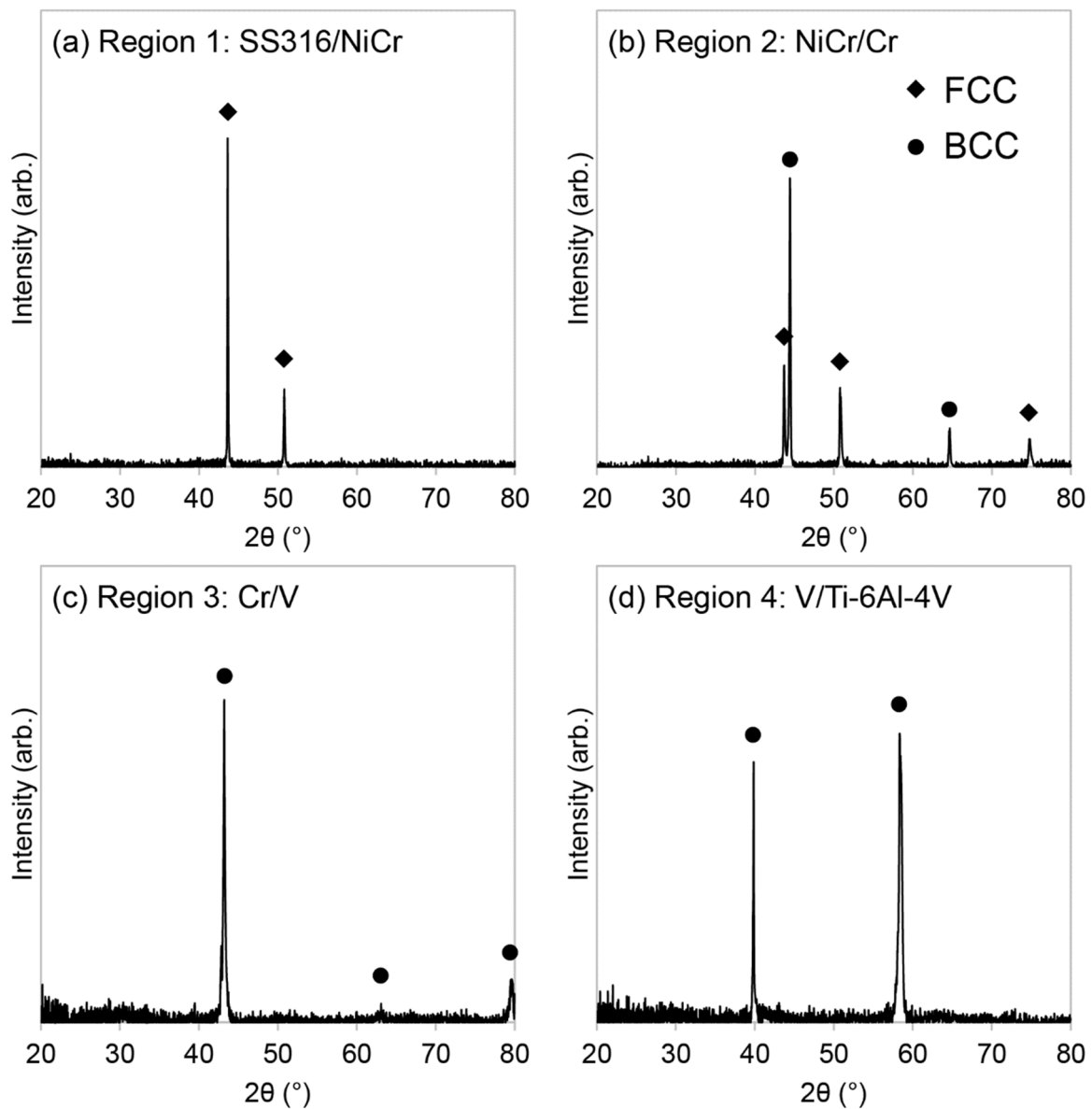


Fig. 7. X-ray diffraction patterns from the four gradient regions in the FGM: (a) Region 1 (SS316/NiCr), (b) Region 2 (NiCr/Cr), (c) Region 3 (Cr/V), and (d) Region 4 (V/Ti-6Al-4V).

bcc-rich region. The elemental compositions and phase fractions for each region are given in Table 3. In addition, the areas examined by EBSD overlap with those examined by EDS, shown in Fig. 6. By examining the two in conjunction, it is evident that there is direct overlap with the fcc-rich regions and the Ni-rich regions, and the bcc-rich regions and the Cr-rich regions. EDS showed no other elemental segregation, so it is unlikely that the low amounts of zero solution are an additional phase.

Vickers microhardness measurements, taken along the height of the FGM, at 2.5 mm intervals, with five measurements at each vertical location, are given in Fig. 9b. In Region 1 (SS316/NiCr), the hardness is relatively constant, with an average hardness of 150 HV. The hardness increases in Region 2 to a peak hardness of 704 HV at 31 mm corresponding the maximum concentration of Cr. The hardness decreased in Regions 3 (Cr/V) and 4 (V/Ti-6Al-4V) to an average of 388 HV. Smaller peaks were observed in both Regions 3 (Cr/V) and 4 (V/Ti-6Al-4V). The presence of these peaks can be attributed to solid solution strengthening as a result of the mixing of the elemental metals and/or alloys in each gradient region. Hardness increases as a result of solid solution

strengthening have been shown for both the Cr/V system [49] and in Ti-6Al-4V/V FGM systems [1,2].

Higher resolution EDS area analysis of the high hardness region revealed the presence of Cr-rich particles with Ni in Region 2 (NiCr/Cr) and particles with Cr and V mixture in Region 3 (Cr/V). Fig. 10 shows SEM images and EDS composition maps of seven selected areas with compositions of 66 wt% Cr/34 wt% Ni (Fig. 10a), 67 wt% Cr/33 wt% Ni (Fig. 10b), 75 wt% Cr/22 wt% Ni/3 wt% V (Fig. 10c), 88 wt% Cr/10 wt% Ni/2 wt% V (Fig. 10d), 91 wt% Ni/3 wt% Ni/6 wt% V (Fig. 10e), 60 wt% Cr/40 wt% V (Fig. 10f), and 40 wt% Cr/60 wt% V (Fig. 10g). These images show how the particle size, morphology, and composition change as a function of overall composition of the analyzed area. Particles were present in six of the seven regions (Fig. 10a–f) imaged with selected EDS composition maps and line scan across a particle shown in Fig. 11 and the EDS point analyses shown in Table 4. In each of the six layers containing particles, the compositions of the particles were significantly different from those of the matrix with higher Cr contents in Region 2 and higher V contents in Region 3. Based on Cr-Ni-V phase diagrams (see Fig. 3) and XRD analyses (see Fig. 7), both the matrix and

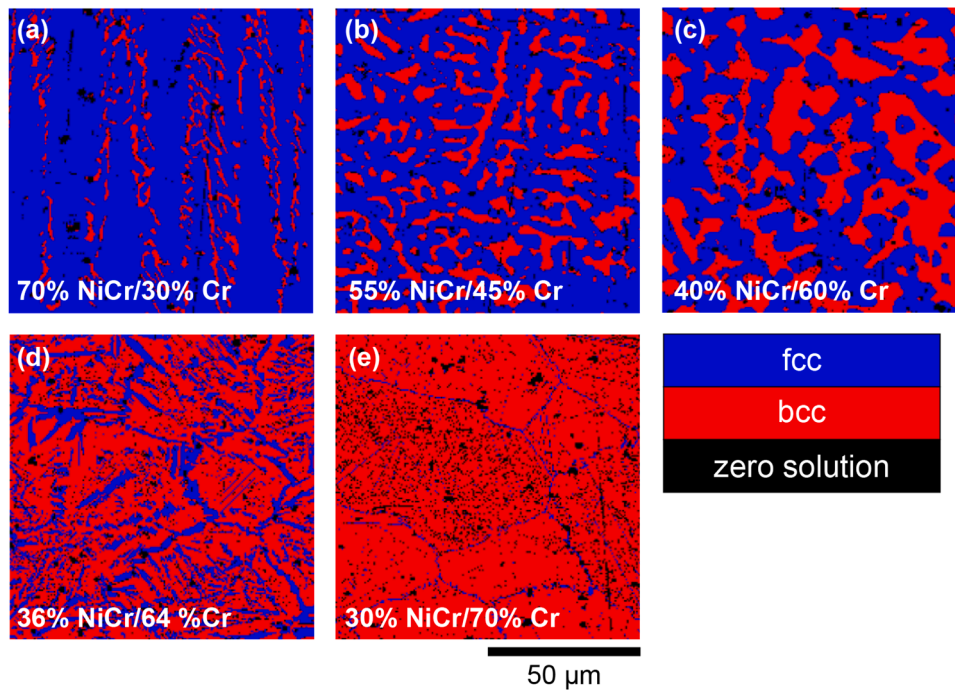


Fig. 8. EBSD phase maps showing the progression from a primarily fcc phase to a primarily bcc phase in Region 2 (NiCr/Cr) of the FGM.

Table 3
EBSD phase amounts (area %) for the five analyzed areas shown in Fig. 8.

	Site (a)	Site (b)	Site (c)	Site (d)	Site (e)
Elemental composition	56 wt% Ni/44 wt % Cr	44 wt% Ni/56 wt % Cr	32 wt% Ni/68 wt % Cr	29 wt% Ni/71 wt% Cr	24 wt% Ni/76 wt% Cr
FCC	87%	71%	58%	29%	3%
BCC	10%	25%	39%	65%	87%
Zero solution (not indexed by EBSD)	3%	4%	3%	6%	10%

particles are bcc phases, i.e., bcc particles in the bcc matrix. It seems that the compositions of particles matched the planned composition of a layer that would be deposited later in the build. For example, the matrix composition of Site (c) with 75 wt% Cr and 22 wt% Ni corresponds to a planned composition for a layer in Region 2 (NiCr/Cr) before V was introduced, but the particle composition contains 32 wt% V and 1 wt% Ni, which corresponds to a composition for a layer in Region 3 (Cr/V). Particle morphologies in Site (a) and Site (b) are mostly spherical. Site (c) and Site (d) have non-spherical particles with many being faceted, while Site (e) and Site (f) show a preference for spherical particle morphologies in grain interiors, with agglomerations near apparent grain boundaries. Section 4.2 will discuss the plausible origin of these particles in more detail.

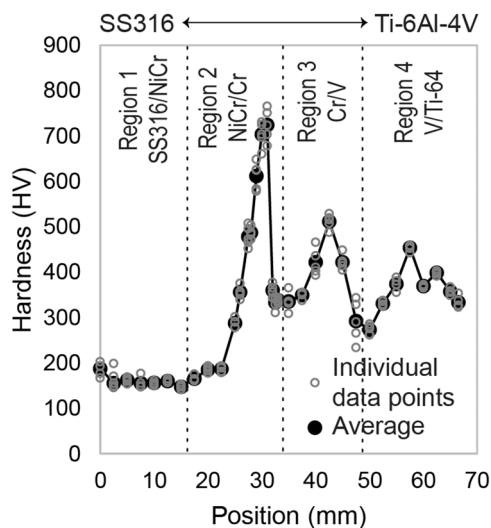


Fig. 9. Vickers microhardness as a function of position along the height of the gradient.

4.2. Computational results and comparison with experimental results

CALPHAD analysis was used to predict the phases and phase compositions along the height of the FGM. The equilibrium calculations were performed at the solidus temperature for each layer of the FGM. The solid lines in the graph in Fig. 12 shows the predicted equilibrium phase fractions where there is an abrupt change from 100% fcc to 100% bcc composition at the transition from Region 2 (NiCr/Cr) to Region 3 (Cr/V). This transition from fcc to bcc agrees with experimental observations, however, there is a slight disagreement in that the equilibrium calculations predict an abrupt transition, while EDS and EBSD analyses showed a gradual transition from fully fcc to fully bcc over the span of 30 wt% of Ni, with a two-phase fcc+bcc composition in Region 2 (NiCr/Cr). The Scheil simulation results, shown as dashed lines in Fig. 12, predict a gradual change in phase fraction over a span of 50 wt% Ni, with an fcc+bcc region in agreement with where the two-phase region was observed experimentally (Fig. 8). The symbols indicating the experimentally determined phase fraction of bcc in Fig. 12 show that the Scheil simulation results are in better agreement with the experimental results.

The formation of particles shown in Fig. 10 is puzzling because both particles and the matrix seem to be the bcc phase as mentioned above, but there is no bcc miscibility gap in the system. As discussed above and shown in Table 4, the particles have higher Cr content in Sites (a) and (b)

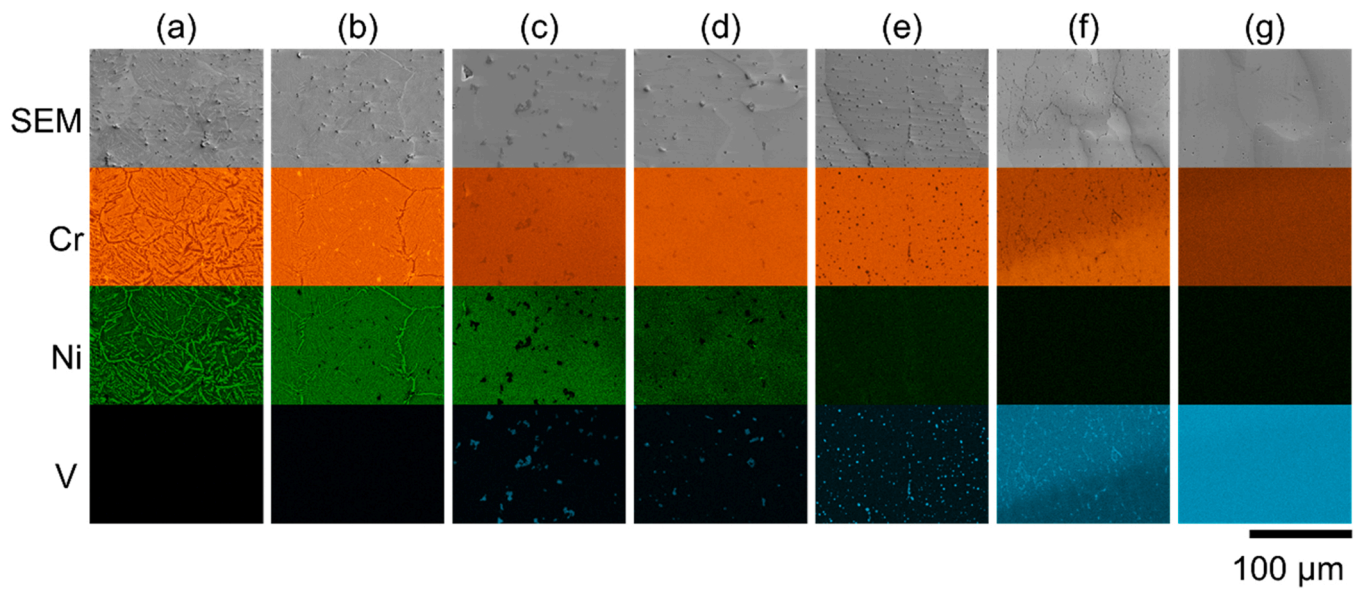


Fig. 10. EDS maps of selected areas in Regions 2 (NiCr/Cr) and 3 (Cr/V) that show the change in microstructure between these areas. The small particles in these images are Cr- and Ni-rich in the NiCr/Cr region (a, b), and Cr- and V-rich in the Cr/V region (c, d, e, f) of the FGM. Starting in the region pictured in (g), no particles were present. Matrix and particle composition data are given in [Table 4](#).

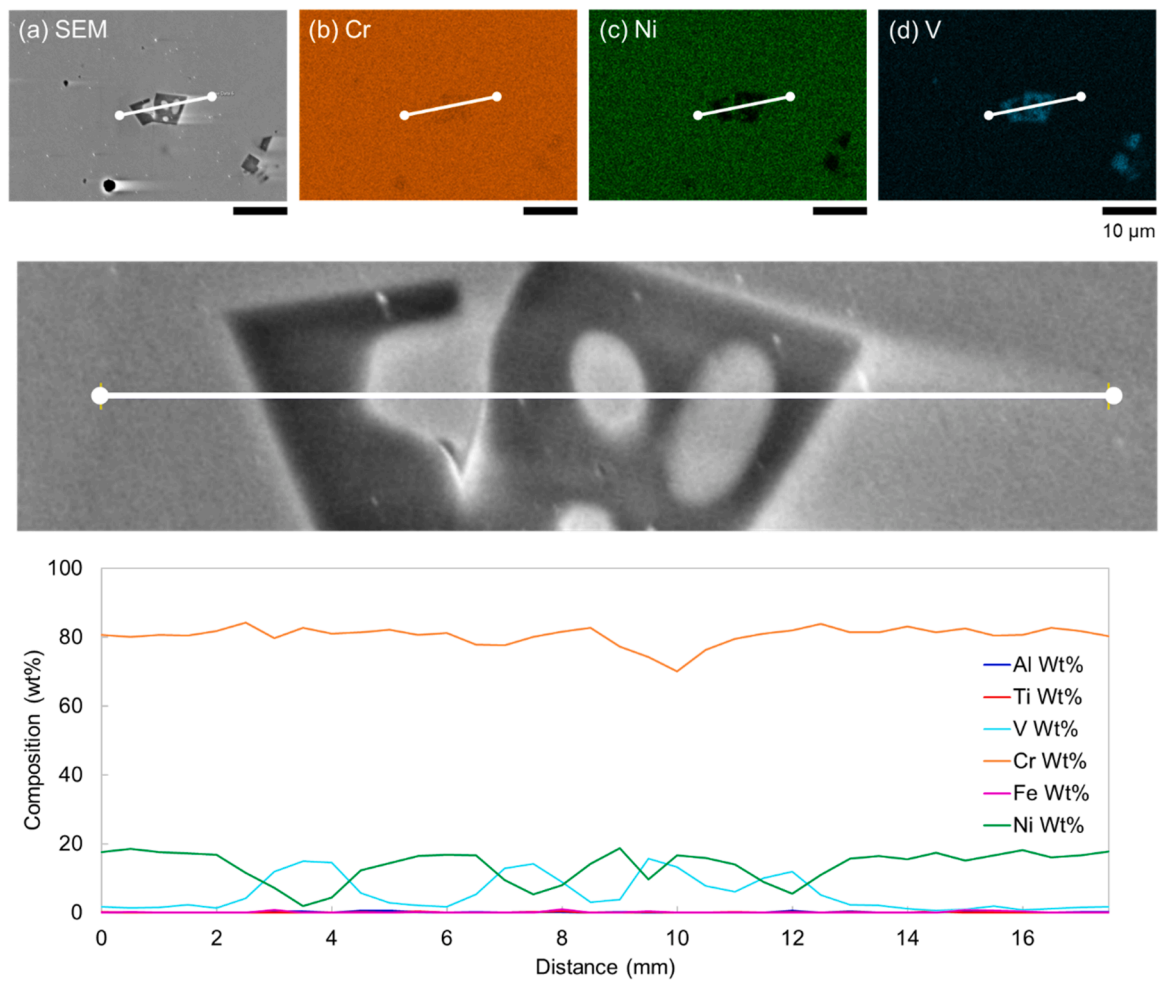


Fig. 11. (a) SEM image and (b–d) EDS composition maps of a selected particle from Site C in [Fig. 10](#). A line scan was taken across the particle to show the composition changes between the particle and the matrix and within the particle itself.

Table 4

Matrix and particle composition data, and particle size data, for the seven sites shown in Fig. 10. Note that there is a non-zero interaction volume, which is a function of material and imaging conditions, when EDS data are acquired; therefore, it is expected that some of the matrix composition is included in the measured composition of the Cr/V-rich particles. Liquidus temperatures are computed using the thermodynamic database from Choi et al. [41].

		wt% Cr	wt% Ni	wt% V	Median Particle Size (μm^2)	Mean Particle Size (μm^2)	Liquidus Temp. (K)	BCC Solvus Temp. (K)
Site (a)	Matrix	66	34	0	0.91	1.37	1790	1525 (FCC)
	Particles	90	10	0			2071	1340 (FCC)
Site (b)	Matrix	67	33	0	0.95	1.38	1802	1511 (FCC)
	Particles	85	15	0			2015	1388 (FCC)
Site (c)	Matrix	75	22	3	7.60	10.9	1935	1409 (FCC)
	Particles	67	1	32			2171	906 (σ)
Site (d)	Matrix	88	10	2	3.15	4.76	2072	1325 (FCC)
	Particles	82	2	16			2159	991 (σ)
Site (e)	Matrix	91	3	6	0.61	1.08	2148	1110 (FCC)
	Particles	36	0	64			2182	–
Site (f)	Matrix	60	0	40	0.51	0.76	2181	–
	Particles	50	0	50			2182	–
Site (g)	Matrix	40	0	60	–	–	2182	–
	Particles	–	–	–				–

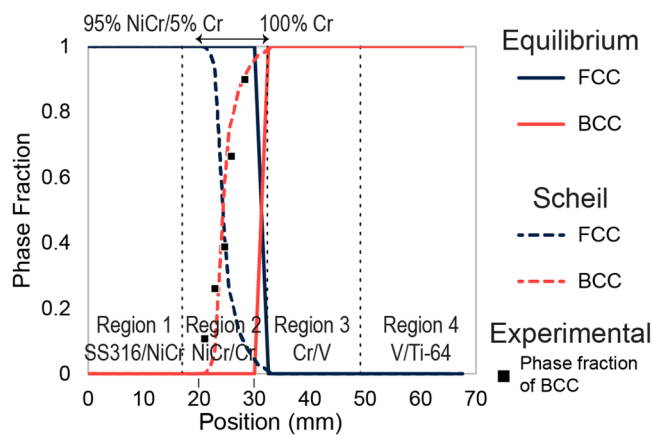


Fig. 12. Equilibrium (solid lines) and Scheil solidification (dashed lines) predicted phase compositions as a function position along the height of the FGM. The square symbols indicate the phase fraction of bcc as determined through experimental EBSD analysis. The arrows above the graph indicate the composition ranges in which the transition from fcc to bcc is predicted by Scheil solidification methods of analysis.

and higher V content in Sites (c)–(f) than the matrix, which are in accordance with the deposited composition later along the gradient path in Region 2 (NiCr/Cr) and Region 3 (Cr/V). We thus hypothesize that the particles were introduced by mixing of pure Cr and V powders with previously deposited layers, which were partially remelted. As Region 2 and 3 reside in the Cr–Ni–V ternary system, the ternary equilibrium isotherm, liquidus projection, and feasibility diagram shown in Fig. 3 can be used to rationalize our hypothesis.

The melting temperatures of Ni–20Cr, Cr, V are listed in Table 2 and the melting temperatures of various particles and matrixes, i.e., their liquidus, shown in Table 4. Furthermore, the bcc solvus temperatures of the particles and matrixes are calculated and included in Table 4. Note that the thermodynamic database from Choi et al. [41] accepts a description of pure Cr that adopts a melting point of 2180 K, rather than the most recently accepted melting point of 2136 K, as discussed by Obaied et al. [47]. In addition, the database from Choi uses binary interaction parameters for Cr–V that produce a cigar-shaped liquidus [50], while the critical review of the Cr–V system by Smith, Bailey, and Carlsson suggests an azeotropic minimum in the liquidus [51]. The thermodynamic database from Choi et al. is used for the present analysis as it is the only available model for the ternary Cr–Ni–V system. Incorporating the new unary description of Cr with the corrected melting point and remodeling the Cr–V binary system is necessary to correct this

discrepancy, but is outside the scope of the present work.

From the liquidus projection in Fig. 3b, bcc is the primary crystallization phase in the composition range of the particles and matrixes in the sites shown in Fig. 10. Fig. 3c depicts that both Scheil solidification and equilibrium calculations from 1000 K to 2200 K show less than 10% of any deleterious phases. It is self-evident that no deleterious phases would form in Sites (a), (b), (f), and (g) as they are in binary Cr–Ni and Cr–V systems, respectively. In Sites (c) and (d), the matrix and particles are stable in equilibrium as bcc between the liquidus temperature and the solvus temperatures given in Table 4. The particles in Sites (c) and (d) are stable until below 1000 K, where the σ phase becomes favorable, but the slow transformation kinetics of the σ phase and the Ni–V-rich compositions of the σ phase eliminate σ phase as a candidate for the particles given the compositions shown in Fig. 11 [39]. The particles in Site (e) are stable down to room temperature, as indicated by the lack of a bcc solvus temperature in Table 4. The Scheil simulations for the binary Cr–Ni and Cr–V systems are shown in Fig. 12, and the small amounts of V into Cr–Ni and Ni into Cr–V give similar results. Therefore, we conclude that the particles observed in Fig. 10 are the bcc phase, the same as the matrix. Next, we postulate how the bcc particles may form.

Table 4 shows that the liquidus temperatures of the particles are higher than those of the matrixes at the same location by up to 281 K. When the Cr or V powders are added, the droplets with higher melting temperature will mix with the re-melted layers in the existing build with lower melting temperatures. The heat of those droplets will quickly be conducted to the re-melted layers with lower temperatures. Some droplets will thus nucleate and solidify to form bcc phase with their composition partially frozen in before they have time to mix with the re-melted layers due to the much faster heat conduction rate than the diffusion rates of Cr and V elements. Assuming the particles follow the solidification path to the azeotropic minimum in the Cr–V liquidus suggested by Smith, Bailey, and Carlsson [51], nucleated particles near Site (c) and Site (d) are able to grow because the composition of the solid (bcc) is close to the composition of the liquid near the azeotropic minimum. The faceted morphologies found in Sites (c) and (d) support the hypothesis that these particles were able to grow, leading to the larger particle sizes in these sites (10.9 μm^2 and 4.76 μm^2 for Sites (c) and (d), respectively) compared to the particles at other sites in Fig. 10 (sizes 1.37 μm^2 , 1.38 μm^2 , 1.08 μm^2 , and 0.76 μm^2 for Sites (a), (b), (e), and (f), respectively) that show predominantly spherical morphologies that suggest the particles formed more like frozen droplets from the upper layer. The bcc particles will stay as bcc as it is the stable phase in the Cr–V system, and the relative low bcc solvus temperatures in the Cr–Ni system as shown in Table 4 may prevent the formation of fcc or σ phase. This issue may be resolved by pre-mixing powders to lower their melting temperatures or optimization of processing parameters in the future.

5. Conclusions

In this study, computational analysis was used to design a feasible compositional pathway through which to join SS316 and Ti-6Al-4V, through the introduction of intermediate elements/alloys, that avoided detrimental phase formation. Through the use of DED AM with the real-time variation of volume fractions of two powders at a time, the designed path, grading from 100% SS316 to 100% NiCr to 100% Cr to 100% V to 100% Ti-6Al-4V, was fabricated. The FGMs were experimentally characterized to analyze the phase fraction, microstructural changes, and mechanical behavior along the entire gradient path. The primary finds of the study are as follows:

- Equilibrium and Scheil analysis of the phases of various ternary systems indicated that Ni, Cr, and V were all necessary intermediate elements in order to fabricate an FGM of SS316 and Ti-6Al-4V with no detrimental phase formation. This allowed for informed design of a SS316/NiCr/Cr/V/Ti-6Al-4V FGM with no detrimental phases.
- Experimental analysis in the NiCr/Cr gradient region showed compositional fluctuations in the EDS line scans indicative of multiple phases. XRD and EBSD analysis of this region confirmed that the elemental segregation was related to the phase transition from fcc to bcc in this region.
- Both equilibrium calculations and Scheil-Gulliver simulations correctly predicted a transition from fcc to bcc phase within the gradient region where this transition was observed experimentally. However, the equilibrium calculations showed a sharp transition at the interface between the NiCr/Cr gradient region and the Cr/V gradient region while the Scheil simulations showed a gradual transition from fcc to bcc over the entire Cr-rich region of the NiCr/Cr gradient region, and the composition range for this transition predicted by Scheil simulations was in strong agreement with the experimental results.

CRedit authorship contribution statement

Lourdes D. Bobbio: Writing – original draft, Validation, Investigation, Formal analysis, Data curation. **Brandon Bocklund:** Formal analysis, Investigation, Software, Validation, Visualization, Writing – review & editing, Data curation. **Emrah Simsek:** Resources. **Ryan T. Ott:** Resources. **Matt J. Kramer:** Resources. **Zi-Kui Liu:** Conceptualization, Funding acquisition, Methodology, Writing – review & editing. **Allison M. Beese:** Conceptualization, Funding acquisition, Methodology, Writing – review & editing, Supervision, Resources, Project administration.

Declaration of Competing Interest

The authors declare that they have no known competing financial interests or personal relationships that could have appeared to influence the work reported in this paper.

Acknowledgments

Sample fabrication (ES, RTO, MJK) was performed at Iowa State University and Ames Laboratory, which is operated by ISU for the U.S. DOE under contract DE-AC02-07CH11358. LDB was supported by an NDSEG Fellowship. BB was supported by a NASA Space Technology Research Fellowship (Grant 90NSSC18K1168) and an NSF National Research Trainee Fellowship (Grant DGE-1449785). We gratefully acknowledge funding from NSF (Grant CMMI-2050069).

References

- [1] A. Reichardt, R.P. Dillon, J. Paul, A.A. Shapiro, B.W. Mcenerney, T. Momose, P. Hosemann, Development and characterization of Ti-6Al-4V to 304L stainless

- steel gradient components fabricated with laser deposition additive manufacturing, *Mater. Des.* 104 (2016) 404–413, <https://doi.org/10.1016/j.matdes.2016.05.016>.
- [2] D.C. Hofmann, S. Roberts, R. Otis, J. Kolodziejska, R.P. Dillon, J. Suh, A.A. Shapiro, Z.-K. Liu, J.-P. Borgonia, Developing gradient metal alloys through radial deposition additive manufacturing, *Sci. Rep.* 4 (2014) 5357, <https://doi.org/10.1038/srep05357>.
- [3] T. Niendorf, S. Leuders, A. Riemer, F. Brenne, T. Troster, H.A. Richerd, D. Schwarze, Functionally graded alloys obtained by additive manufacturing, *Adv. Eng. Mater.* 16 (2014) 857–861.
- [4] B. Heer, A. Bandyopadhyay, W. Keck, Compositionally graded magnetic-nonmagnetic bimetallic structure using laser engineered net shaping, *Mater. Lett.* 216 (2018) 16–19, <https://doi.org/10.1016/j.matlet.2017.12.129>.
- [5] S.M. Kumar, A.R. Kannan, N.P. Kumar, R. Pramod, N.S. Shanmugam, A.S. Vishnu, S.G. Channabasavanna, Microstructural features and mechanical integrity of wire arc additive manufactured SS321 / inconel 625 functionally gradient material, *J. Mater. Eng. Perform.* 69 (2021) 1247–1258, <https://doi.org/10.1007/s11665-021-05617-3>.
- [6] N. Özdemir, B. Bilgin, Interfacial properties of diffusion bonded Ti-6Al-4V to AISI 304 stainless steel by inserting a Cu interlayer, *Int. J. Adv. Manuf. Technol.* 41 (2009) 519–526, <https://doi.org/10.1007/s00170-008-1493-6>.
- [7] M. Ghosh, S. Chatterjee, B. Mishra, The effect of intermetallics on the strength properties of diffusion bonds formed between Ti-5.5Al-2.4V and 304 stainless steel, *Mater. Sci. Eng. A* 363 (2003) 268–274, [https://doi.org/10.1016/S0921-5093\(03\)00649-X](https://doi.org/10.1016/S0921-5093(03)00649-X).
- [8] H.C. Dey, M. Ashfaq, A.K. Bhaduri, K.P. Rao, Joining of titanium to 304L stainless steel by friction welding, *J. Mater. Process. Technol.* 209 (2009) 5862–5870, <https://doi.org/10.1016/j.jmatprotec.2009.06.018>.
- [9] G.B. Kale, R.V. Patil, P.S. Gawade, Interdiffusion studies in titanium-304 stainless steel system, *J. Nucl. Mater.* 257 (1998) 44–50.
- [10] S. Kundu, S. Sam, S. Chatterjee, Interface microstructure and strength properties of Ti-6Al-4V and microduplex stainless steel diffusion bonded joints, *Mater. Des.* 32 (2011) 2997–3003, <https://doi.org/10.1016/j.matdes.2010.12.052>.
- [11] Y. Gao, T. Tsumura, K. Nakata, Dissimilar welding of titanium alloys to steels, *Trans. Join. Weld. Res. Inst.* 41 (2012) 7–12.
- [12] M. Ghosh, S. Chatterjee, Diffusion bonded transition joints of titanium to stainless steel with improved properties, *Mater. Sci. Eng. A* 358 (2003) 152–158, [https://doi.org/10.1016/S0921-5093\(03\)00298-3](https://doi.org/10.1016/S0921-5093(03)00298-3).
- [13] M. Ghosh, S. Chatterjee, Characterization of transition joints of commercially pure titanium to 304 stainless steel, *Mater. Charact.* 48 (2002) 393–399, [https://doi.org/10.1016/S1044-5803\(02\)00306-6](https://doi.org/10.1016/S1044-5803(02)00306-6).
- [14] H. Sahasrabudhe, R. Harrison, C. Carpenter, A. Bandyopadhyay, Stainless steel to titanium bimetallic structure using LENS, *Addit. Manuf.* 5 (2015) 1–8, <https://doi.org/10.1016/j.addma.2014.10.002>.
- [15] L.D. Bobbio, R.A. Otis, J.P. Borgonia, R.P. Dillon, A.A. Shapiro, Z.-K. Liu, A. M. Beese, Additive manufacturing of a functionally graded material from Ti-6Al-4V to invar: experimental characterization and thermodynamic calculations, *Acta Mater.* 127 (2017) 133–142, <https://doi.org/10.1016/j.actamat.2016.12.070>.
- [16] I. Shishkovsky, F. Missemmer, N. Kakovkina, I. Smurov, Intermetallics synthesis in the Fe-Al system via layer by layer 3D laser cladding, *Crystals* 3 (2013) 517–529, <https://doi.org/10.3390/cryst3040517>.
- [17] S. Lotfian, G. Rolink, A. Weisheit, M. Palm, Chemically graded Fe-Al/steel samples fabricated by laser metal deposition, *MRS Adv.* 2 (2017) 1393–1398, <https://doi.org/10.1557/adv.2017.124>.
- [18] N.K. Adomako, J.O. Kim, J.H. Kim, Microstructural evolution and mechanical properties of laser beam welded joints between pure V and 17-4PH stainless steel, *Mater. Sci. Eng. A* 753 (2019) 208–217, <https://doi.org/10.1016/j.msea.2019.03.036>.
- [19] K. Liu, Y. Li, C. Xia, J. Wang, Effect of bonding time on interfacial microstructure and shear strength of vacuum diffusion bonding super-Ni/NiCr laminated composite to Ti-6Al-4V joint without interlayer, *Vacuum* 143 (2017) 195–198, <https://doi.org/10.1016/j.vacuum.2017.06.025>.
- [20] Y. Zhang, D.Q. Sun, X.Y. Gu, Z.Z. Duan, H.M. Li, Nd:YAG pulsed laser welding of TC4 Ti alloy to 301L stainless steel using Ta/V/Fe composite interlayer, *Mater. Lett.* 212 (2018) 54–57, <https://doi.org/10.1016/j.matlet.2017.10.057>.
- [21] W. Li, S. Karnati, C. Kriewall, F. Liou, J. Newkirk, K.M.B. Taminger, W.J. Seufzer, Fabrication and characterization of a functionally graded material from Ti-6Al-4V to SS316 by laser metal deposition, *Addit. Manuf.* 14 (2017) 95–104, <https://doi.org/10.1016/j.addma.2016.12.006>.
- [22] L.D. Bobbio, B. Bocklund, R. Otis, J.P. Borgonia, R.P. Dillon, A.A. Shapiro, B. McEnerney, Z.-K. Liu, A.M. Beese, Characterization of a functionally graded material of Ti-6Al-4V to 304L stainless steel with an intermediate V section, *J. Alloy. Compd.* 742 (2018) 1031–1036, <https://doi.org/10.1016/j.jallcom.2018.01.156>.
- [23] N.K. Adomako, S. Noh, C.S. Oh, S. Yang, J.H. Kim, Laser deposition additive manufacturing of 17-4PH stainless steel on Ti-6Al-4V using V interlayer, *Mater. Res. Lett.* 7 (2019) 259–266, <https://doi.org/10.1080/21663831.2019.1596989>.
- [24] S.R. Elmi Hosseini, K. Feng, P. Nie, K. Zhang, J. Huang, Z. Li, H. Kokawa, B. Guo, S. Xue, Interlayer thickening for development of laser-welded Ti-SS joint strength, *Opt. Laser Technol.* 112 (2019) 379–394, <https://doi.org/10.1016/j.optlastec.2018.11.022>.
- [25] X. Chen, J. Han, J. Wang, Y. Cai, G. Zhang, L. Lu, Y. Xin, Y. Tian, A functionally graded material from TC4 to 316L stainless steel fabricated by double-wire + arc additive manufacturing, *Mater. Lett.* 300 (2021), 130141, <https://doi.org/10.1016/j.matlet.2021.130141>.

- [26] S.M. Dubiel, J. Cieslak, Sigma-phase in Fe-Cr and Fe-V alloy systems and its physical properties, *Crit. Rev. Solid State Mater. Sci.* 36 (2011) 191–208, <https://doi.org/10.1080/10408436.2011.589232>.
- [27] B.F.O. Costa, J. Cieslak, S.M. Dubiel, Kinetics of σ -phase formation in equiatomic cold-rolled Fe-V alloys, *Mater. Chem. Phys.* 143 (2013) 19–25, <https://doi.org/10.1016/j.matchemphys.2013.07.020>.
- [28] L.D. Bobbio, B. Bocklund, A. Reichardt, R. Otis, J.P. Borgonia, R.P. Dillon, A. A. Shapiro, B.W. McEnerney, P. Hosemann, Z.-K. Liu, A.M. Beese, Analysis of formation and growth of the σ phase in additively manufactured functionally graded materials, *J. Alloy. Compd.* 814 (2020), 151729, <https://doi.org/10.1016/j.jallcom.2019.151729>.
- [29] T. Kirk, E. Galvan, R. Malak, R. Arroyave, Computational design of gradient paths in additively manufactured functionally graded materials, *J. Mech. Des.* 140 (2018), <https://doi.org/10.1115/1.4040816>.
- [30] O.V. Eliseeva, T. Kirk, P. Samimi, R. Malak, R. Arróyave, A. Elwany, I. Karaman, Functionally graded materials through robotics-inspired path planning, *Mater. Des.* 182 (2019), 107975, <https://doi.org/10.1016/j.matdes.2019.107975>.
- [31] B. Bocklund, L.D. Bobbio, R.A. Otis, A.M. Beese, Z.K. Liu, Experimental validation of Scheil–Gulliver simulations for gradient path planning in additively manufactured functionally graded materials, *Materialia* 11 (2020), 100689, <https://doi.org/10.1016/j.mtla.2020.100689>.
- [32] L. Kaufman, H. Bernstein, *Computer Calculation of Phase Diagram*, Academic Press Inc., New York, 1970.
- [33] Z.K. Liu, First-principles calculations and CALPHAD modeling of thermodynamics, *J. Phase Equilibria Diffus.* 30 (2009) 517–534, <https://doi.org/10.1007/s11669-009-9570-6>.
- [34] M. Hillert, The compound energy formalism, *J. Alloy. Compd.* 320 (2001) 161–176, [https://doi.org/10.1016/S0925-8388\(00\)01481-X](https://doi.org/10.1016/S0925-8388(00)01481-X).
- [35] R. Otis, Z.-K. Liu, pycalphad: CALPHAD-based computational thermodynamics in python, *J. Open Res. Softw.* 5 (2017) 1, <https://doi.org/10.5334/jors.140>.
- [36] J. De Keyser, G. Cacciamani, N. Dupin, P. Wollants, Thermodynamic modeling and optimization of the Fe–Ni–Ti system, *Calphad Comput. Coupling Phase Diagr. Thermochem.* 33 (2009) 109–123, <https://doi.org/10.1016/j.calphad.2008.10.003>.
- [37] S. Wang, K. Wang, G. Chen, Z. Li, Z. Qin, X. Lu, C. Li, Thermodynamic modeling of Ti-Fe-Cr ternary system, *Calphad* 56 (2017) 160–168, <https://doi.org/10.1016/j.calphad.2016.12.007>.
- [38] B. Bocklund, L.D. Bobbio, R.A. Otis, A.M. Beese, Z.-K. Liu, pycalphad-scheil: 0.1.2, 2020. DOI: [10.5281/zenodo.3630657](https://doi.org/10.5281/zenodo.3630657).
- [39] P.E.A. Turchi, L. Kaufman, Z.-K. Liu, Modeling of Ni-Cr-Mo based alloys: part II - kinetics, *Calphad Comput. Coupling Phase Diagr. Thermochem.* 31 (2007) 237–248.
- [40] J. Miettinen, Thermodynamic reassessment of Fe-Cr-Ni system with emphasis on the iron-rich corner, *Calphad* 23 (1999) 231–248, [https://doi.org/10.1016/S0364-5916\(99\)00027-9](https://doi.org/10.1016/S0364-5916(99)00027-9).
- [41] W.M. Choi, Y.H. Jo, D.G. Kim, S.S. Sohn, S. Lee, B.J. Lee, A thermodynamic description of the Co-Cr-Fe-Ni-V system for high-entropy alloy design, *Calphad Comput. Coupling Phase Diagr. Thermochem.* 66 (2019), 101624, <https://doi.org/10.1016/j.calphad.2019.05.001>.
- [42] J. Huang, Y. Wang, J. Wang, X.-G. Lu, L. Zhang, Thermodynamic assessments of the Ni-Cr-Ti system and atomic mobility of its Fcc phase, *J. Phase Equilibria Diffus.* 39 (2018) 597–609, <https://doi.org/10.1007/s11669-018-0650-3>.
- [43] G. Ghosh, Thermodynamic and kinetic modeling of the Cr-Ti-V system, *J. Phase Equilibria Diffus.* 23 (2002) 310–328, <https://doi.org/10.1361/105497102770331569>.
- [44] C.C. Zhao, S.Y. Yang, Y. Lu, Y.H. Guo, C.P. Wang, X.J. Liu, Experimental investigation and thermodynamic calculation of the phase equilibria in the Fe-Ni-V System, *Calphad* 46 (2014) 80–86, <https://doi.org/10.1016/j.calphad.2014.02.004>.
- [45] C. Guo, C. Li, X. Zheng, Z. Du, Thermodynamic modeling of the Fe-Ti-V system, *Calphad Comput. Coupling Phase Diagr. Thermochem.* 38 (2012) 155–160, <https://doi.org/10.1016/j.calphad.2012.06.010>.
- [46] L. Zou, C. Guo, C. Li, Z. Du, Experimental investigation and thermodynamic modeling of the Ni-Ti-V system, *Calphad Comput. Coupling Phase Diagr. Thermochem.* 64 (2019) 97–114, <https://doi.org/10.1016/j.calphad.2018.11.006>.
- [47] A. Obaied, B. Bocklund, S. Zomorodpoosh, L. Zhang, R. Otis, Z.K. Liu, I. Roslyakova, Thermodynamic re-assessment of pure chromium using modified segmented regression model, *Calphad Comput. Coupling Phase Diagr. Thermochem.* 69 (2020), 101762, <https://doi.org/10.1016/j.calphad.2020.101762>.
- [48] L.D. Bobbio, B. Bocklund, Z.-K. Liu, A.M. Beese, Tensile behavior of stainless steel 304L to Ni-20Cr functionally graded material: experimental characterization and computational simulations, *Materialia* 18 (2021), 101151, <https://doi.org/10.1016/j.mtla.2021.101151>.
- [49] O.N. Carlson, D.T. Eash, A.L. Eustice, *Vanadium-tantalum and vanadium-chromium alloy systems*, Ames Lab. Tech. Rep. (1959) 277–293.
- [50] B.-J. Lee, A thermodynamic evaluation of the Fe - Cr - V system / eine thermodynamische bewertung des systems Fe-Cr-V, *Int. J. Mater. Res.* 83 (1992) 292–299, <https://doi.org/10.1515/ijmr-1992-830502>, 292–200.
- [51] J.F. Smith, D.M. Bailey, O.N. Carlson, The Cr-V (Chromium-vanadium) System, *Bull. Alloy Phase Diagr.* 2 (1982) 469–473, <https://doi.org/10.1007/BF02876166>.